Rapid Response Solar Blind Deep UV Photodetector with High Detectivity Based On Graphene:N/βGa$_2$O$_3$:N/GaN p-i-n Heterojunction Fabricated by a Reversed Substitution Growth Method

Yurui Han,[1] Yuefei Wang,[1] Danyang Xia,[1] Shihao Fu,[1] Chong Gao,[1] Jiangang Ma,[1] Haiyang Xu,[1] Bingsheng Li,[1,*] Aidong Shen,[2] Yichun Liu[1]

[1]Key Laboratory of UV Light Emitting Materials and Technology, Ministry of Education, Northeast Normal University, Changchun 130024, China (*Authors to whom correspondence should be addressed, e-mail: libs@nenu.edu.cn).

[2]Department of Electrical Engineering, The City College of New York, New York, NY 10031 USA

JOSarXiv.202303.0003V1

Abstract

We report a high-detectivity solar-blind deep UV photodetector with a fast response speed, based on a nitrogen-doped graphene/βGa$_2$O$_3$/GaN p-i-n heterojunction, in which the i layer of βGa$_2$O$_3$ was obtained by reversed substitution growth with oxygen replacing nitrogen in the GaN matrix. XPS demonstrated the Fermi level of βGa$_2$O$_3$ to be 0.2 eV lower than the central level of the forbidden band, indicating that the dominant carriers are holes. XRD shows that the transformation of GaN into (-201) preferred-orientation βGa$_2$O$_3$ occurs above 900 ^{o}C in an oxygen ambient. The heterojunction shows enhanced self-powered solar blind detection ability with a response time of 3.2 μs (rise)/0.02 ms (delay) and a detectivity exceeding 10^{12} Jones. Under a bias of -5 V, the photoresponsivity is 8.3 A/W with a high I_{light}/I_{dark} ratio of over 10^6 and a detectivity of ~9 × 10^{14} Jones. The excellent performance of the device is attributed to two factors. Firstly, its continuous conduction band without a potential energy barrier, and the larger built-in potential in the heterojunction because Fermi energy level shifts downward in βGa$_2$O$_3$. Secondly, an enhanced built-in electric field in the βGa$_2$O$_3$ due to introducing p-type graphene with a high hole concentration of up to ~10^{20} cm^{-3}.

Introduction

Ultraviolet (UV) radiation significantly impacts human social life, despite accounting for only a small part of solar radiation. Positively, it aids in producing vitamin D, killing bacteria, and so on. However, excessive radiation can hasten aging and cause harm to crops and structures.[1] The most harmful for humans is the solar-

blind deep UV (DUV) region in a wavelength range of λ~200–280 nm (named UVC). The human body will be injured if the radiation energy per second exceeds 10^2 mJ/cm^2.[2] Thus, photodetectors (PDs) for solar-blind radiation have attracted lots of attention. Additionally, photodetectors operating in the UVC region have exhibited significant potential for applications including missile warning systems, fire alarms, environmental monitoring, and space-to-space communications, because they avoid interference from solar radiation.[3-7] Currently, PDs based on the Einstein photoelectric effect are mostly employed to convert DUV radiation into electrical signals for monitoring purposes. Commercial solar-blind PDs mainly comprise photomultiplier tubes (PMTs) and Si-based photodiodes. The former require a high external bias voltage and a vacuum environment, which makes the devices bulky and cumbersome to use in outdoor settings. In the latter, Si has a band gap of 1.12 eV, which necessitates the use of an optical filter to exclude wavelengths other than UV. A new route to fabricate UV PDs has been explored extensively in recent years, based on wide-bandgap semiconductors including $Al_xGa_{1-x}N$ (E_g 3.4–6.2 eV), $Mg_xZn_{1-x}O$ (E_g 3.3–7.8 eV), diamond (E_g 5.5 eV), and βGa_2O_3 (E_g 4.4–5.1 eV), which are easy to integrate with other systems, more stable, and of smaller size than current devices.[8-15]

Despite such attractive potential, the performance of wide-bandgap semiconductor UV PDs needs to be improved further. Compared with PMTs, the detection capabilities of wide-bandgap semiconductor-based UV PDs are still low and do not meet the requirements of practical applications. For example, the detectivity D^* for $Al_xGa_{1-x}N$-based PDs in the solar-blind region is ~10^{12} Jones; for $Al_xGa_{1-x}N$/GaN-based wide spectrum PDs in the visible blind region it is ~10^{13} Jones. These are 1-2 orders lower than that of PMTs ($D^* = 4 \times 10^{14}$ Jones). Improving the performance of devices is still a big challenge in wide-bandgap semiconductor-based UV PDs. In $Al_xGa_{1-x}N$ or $Mg_xZn_{1-x}O$, increasing the Al or Mg mole fractions in the alloy thin films results in the defect density increasing significantly, or in phase separation, leading to severe deterioration in device performance.[16]

At present, βGa_2O_3 appears to be an ideal candidate for solar-blind DUV PD applications, because of its unique energy band structure and its large absorption coefficient above the bandgap. Due to the challenge of p-type realization of βGa_2O_3, most reports of DUV PDs are based on heterojunctions or metal-semiconductor-metal structures. Among them, the βGa_2O_3/GaN heterostructure has promising potential for applications in high performance UV PDs. High structural quality βGa_2O_3/GaN with (-

JOSarXiv.202303.0003V1

201)/(002) crystal plane alignment has been prepared by the epitaxial technique.[17-18] Furthermore, βGa_2O_3 is amenable to wet chemical etching, which is particularly important for device design and fabrication for large-scale production.[19-20] However, in reported βGa_2O_3/GaN heterojunctions, the βGa_2O_3 layer is n-type.[21-22] Considering the energy bandgap alignment between n-type βGa_2O_3 and p-type GaN, there is a potential energy barrier at the interface, which blocks electron transportation, resulting in low detection efficiency. Very recently, we successfully fabricated βGa_2O_3(-201)/GaN(002) heterojunctions and realized ultrahigh detectivity in a wide spectrum range of UVA-UVC by a reversed substitution growth method. The advantages of this method can overcome the disadvantage of low solubility of nitrogen doping due to its high formation energy in oxide semiconductors. The residual N, as an acceptor, led to the Fermi energy level position shiftings downwards, below the central energy line of the βGa_2O_3 band-gap. This is a constructive route for improving the device performance of βGa_2O_3-based heterostructures. Here, compared with based on our previous results, we further optimized the core structure and constructed a p-i-n heterojunction of p-type-graphene/βGa_2O_3/GaN with the introduction of a nitrogen-doped graphene (NGr). The diode device exhibited an excellent rectifying effect with an extremely low dark current of 84 pA (-5 V). The DUV PD showed enhanced self-powered photoresponsivity with a rapid response speed. Under -5 V bias loading, the p-i-n structure realized a high detectivity $D*$ (achieving 8.8×10^{14} Jones), with improved characteristics of spectral selectivity in the solar-blind region.

JOSarXiv.202303.0003V1

Results and Discussion

Figure 1a shows the XRD patterns of as-grown GaN films and GaN annealed at 800 °C, 900 °C, and 1000 °C. Above 900 °C, three new peaks arose, corresponding to (-201), (-402), and (-603) planes of monoclinic βGa_2O_3, respectively (JCPDS Card No.43-1012).[23] The diffraction peak was obviously enhanced at 1000 °C, and the crystallinity of the thin film was greatly improved. However, surface cracking of the βGa_2O_3 film occurred at 1100 ^{o}C due to thermal mismatch between the βGa_2O_3 and GaN. O atoms replaced the surface N atoms of the GaN matrix and formed Ga-O hexagons, as shown in the schematic at the top-right of Figure 1b. A very thin layer of Ga_2O_3 initially had the same atomic arrangement as the GaN matrix at the bottom: a symmetrical hexagonal pattern but with slightly different sizes of hexagons. The newly formed Ga_2O_3 layer acted as a crystal nucleus for Ga_2O_3 growth in the ongoing

processes, with a reversed substitution process of oxygen replacing nitrogen in the GaN matrix. By coincidence, this nucleus layer could be considered as a (-201) plane of βGa_2O_3 or (0002) plane of ε-phase Ga_2O_3, because both of them had the same atomic arrangements in-plane. However, because the temperature was higher than 870 °C, the β-phase was selected preferentially. According to the in-plane lattice constant, as indicated on the right in Figure 1b, the lattice mismatch of βGa_2O_3 and GaN was 5.4%. This was smaller than the 6.6% lattice mismatch between (-201) βGa_2O_3 and sapphire.[24] Thus, βGa_2O_3 thin films with high structural quality can be realized on a GaN matrix via oxygen substitution of nitrogen at a high temperature. So far, this method was used for preparing the βGa_2O_3. However, there were wide variations in structural properties, attributable to the complicated process of transformation from GaN to βGa_2O_3; it involved several aspects, including the phase transition, breaking a Ga–N bond, the formation of Ga–O bonds, and the activation of the residual N atoms as acceptors. Each aspect could be affected by the annealing temperature, thermal oxidation time, annealing method, and characteristics of the GaN precursor. In our experimental processes, we found it was crucial to create Ga-O hexagons on the surface of the GaN matrix at the initial stage of replacing O with N, which induced the next βGa_2O_3 ongoing growth with (-201)-preferred orientation. At present, work is in progress to improve the quality of βGa_2O_3 crystals. Figure 1c shows the surface morphology of the oxidized βGa_2O_3 thin film under SEM. It can be seen that the surface of the film is composed of massive grains linked together, and the film is continuous and dense. For the oxidation of GaN thin films, Yamada et al. confirmed that high-temperature oxidation usually occurred at the penetration dislocation inside GaN films and proposed an oxidation mechanism near the penetration dislocation.[25] That is, GaO_x generated by high-temperature oxidation migrates through the surface, deposits near the penetration dislocation, and eventually forms massive grains. Since the penetration dislocation density of GaN films is usually about 10^8/cm^2, the surface roughness of GaO_x films formed by high-temperature oxidation is relatively high. After oxidation for a period of time, the GaO_x bulk grains generated on the surface gradually increase and merge near the penetration dislocation. Figure 1d shows the cross-sectional image of the Ga_2O_3/GaN heterojunction. There is an apparent interface between the Ga_2O_3 and GaN layers. The thickness of the Ga_2O_3 film was determined by controlling the oxidation substitution time, which is similar to the desired thickness of SiO_2 on a Si matrix

JOSarXiv.202303.0003V1

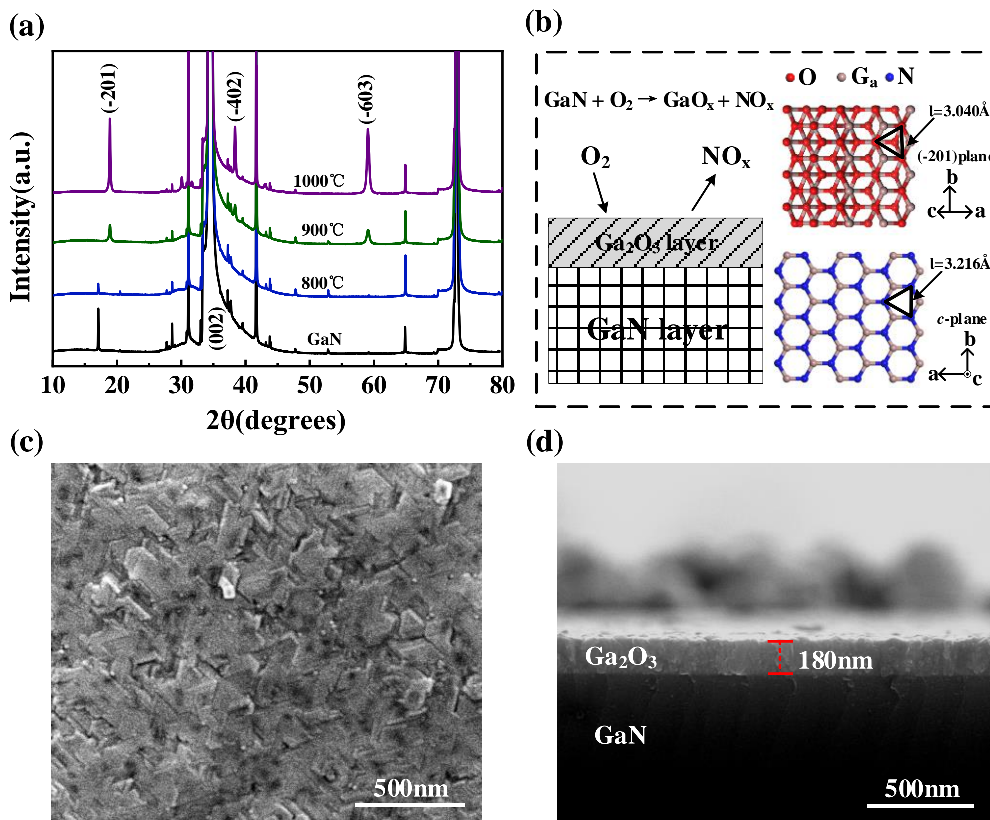

Figure 1. a) XRD spectra of as-grown GaN, and GaN after oxidation at 800 °C, 900 °C, and 1000 °C. b) The model diagram of GaN thermal oxidation to Ga_2O_3 film and the hexagonal pattern of the atomic arrangement in both the (-201) plane of βGa_2O_3 and the (002) plane of GaN. c) SEM image of GaN after oxidation. d) SEM cross section of the interface between Ga_2O_3 and GaN.

Raman spectroscopy was utilized to verify the quality of the N-doped graphene. As shown in **Figure 2**a, the Raman spectrum of NGr consisted of a set of distinct peaks located around 2700 cm^{-1}, 1590 cm^{-1}, and 1350 cm^{-1}, denoted as 2D, G, and D peaks, respectively.[26] The 2D to G peak intensity ratio was ~1.55, indicating the NGr was a monolayer.[27] The D peak was the flawed peak of graphene, which can reveal the disorder caused by graphene due to groups, edges, and defects.[28] There was no D peak in the Raman spectrum of perfect crystals of pure graphene. In N-doped graphene, the introduction of N destroyed the perfect honeycomb structure of the graphene, leading to protrusions of the D peak. The inset shows the SEM images of graphene and βGa_2O_3 thin film. The formation of ohmic contacts between the electrodes and the materials during device fabrication is a crucial factor for high device performance. Graphene easily to forms an ohmic contact with metals due to its high carrier concentration. The *I-V* curve of Al electrodes and our GaN films is shown in Figure 2b. The linear characteristic of the *I-V* curve under dark conditions indicates that the Al electrodes and GaN films were ohmic contact. The dark current of the NGr/βGa_2O_3/GaN p-i-n

JOSarXiv.202303.0003V1

heterojunction structure is shown in Figure 2c. The inset shows the schematic diagram of the device. The *I-V* curve shows the typical rectification characteristics, with a rectification ratio (I_{dark}, 5 V / I_{dark}, -5 V) was 2.93×10^6. These results indicated that the rectification behavior was derived from the NGr/βGa_2O_3/GaN p-i-n heterojunction. The photo/dark ratio (-5 V) of the device was 1.24×10^6 at 254 nm illumination (41 μW/cm^2), showing good photoresponse characteristics, as seen in Figure 2d.

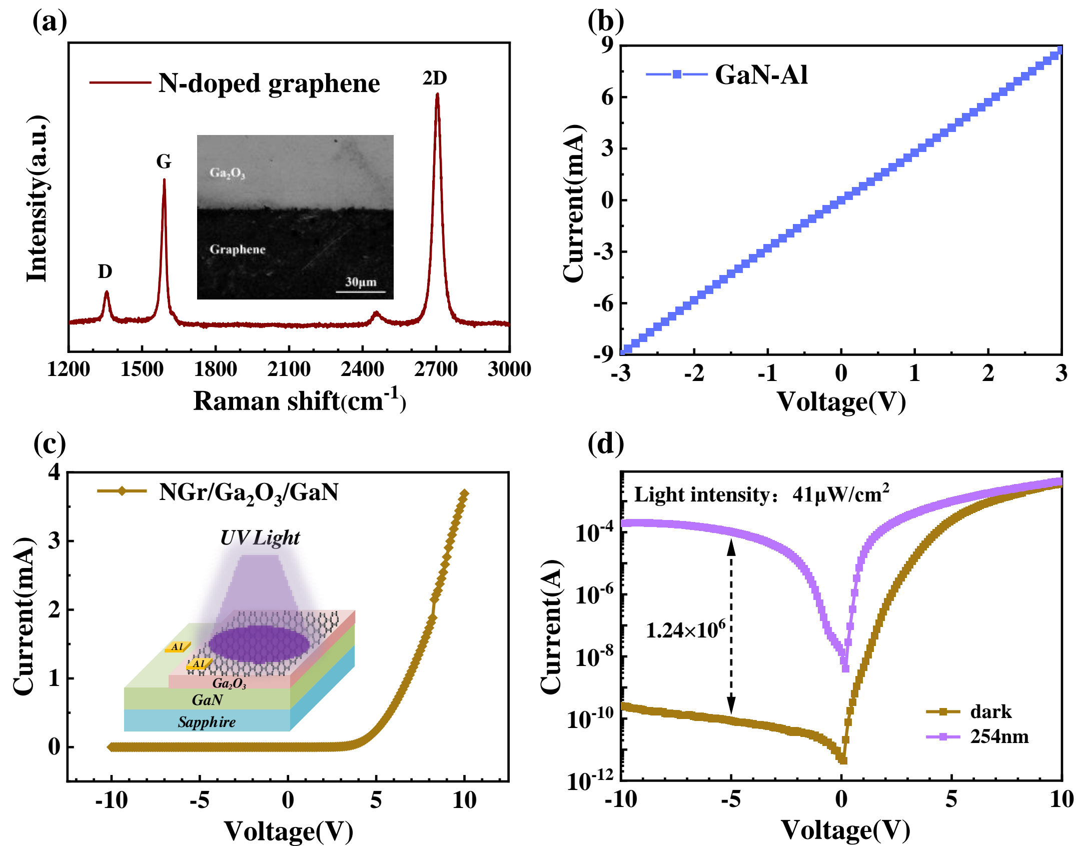

Figure 2. a) N-doped graphene Raman spectroscopy. The inset shows the SEM image of NGr and βGa_2O_3 thin films. b) The *I–V* curve of the GaN with Al electrodes. c) The *I–V* curve of the NGr/βGa_2O_3/GaN p-i-n heterojunction. The inset shows the respective device structures. d) The *I-V* curve of the NGr/βGa_2O_3/GaN p-i-n heterojunction in the dark state and under 254 nm (41 μW/cm^2) light.

Figure 3a shows the *I-T* curve under 254 nm illumination with different intensities at 0 V bias. The photocurrent increased gradually with the increase of light intensity. High-intensity light can produce more photogenerated carriers, thus contributing to a higher photocurrent. The dependence of the photocurrent on the light intensity is summarized in Figure 3b, which can be described by the following power law: $I_{ph} = CP^{\alpha}$, where I_{ph} is the photocurrent, C is constant, P is the light intensity, and α is the intensity law index.[29] The calculated α for the NGr/βGa_2O_3/GaN PD is 0.96, which reflects the existence of trap states and the electron-hole recombination centers in

JOSarXiv.202303.0003V1

βGa_2O_3 and GaN films.[23] Responsivity (R) is a critical parameter for UV PDs, which reflects the photoresponse of PDs to light signals. The R of the photodetectors can be calculated according to the formula $R = I_{ph}/(P_\lambda \cdot S)$, where $I_{ph} = I_{light} - I_{dark}$, with I_{light} and I_{dark} being the currents for the device in light and dark conditions. P_λ and S represent the light intensity of the incident light with wavelength λ and the effective illumination area on the device, respectively.[30] Figure 3c presents the spectral responsivity of Ga_2O_3/GaN and NGr/Ga_2O_3/GaN heterojunction self-powered PDs. The responsivity of the detectors reached a peak at 245 nm and 235 nm, respectively, corresponding to the solar-blind region. Compared with a Ga_2O_3/GaN heterojunction without NGr (for which the responsivity was 1.4 mA/W), the responsivity of NGr/Ga_2O_3/GaN heterojunction was 5.7 times greater, at 8.1 mA/W. The solar blind visible rejection ratio R_{235nm}/R_{400nm} was 7.1×10^3. The rejection ratio R_{235nm}/R_{300nm} was 3.2×10^2. This shows that the detector has very high spectral selectivity. Detectivity (D*) is also an important parameter for evaluating the sensitivity of PDs, which is extracted using the equation $D^* = R/(2qJ)^{1/2}$, where R is the responsivity of the photodetector, q is the elemental charge, and J is the dark current density.[31] At zero bias, the $D*$ of Ga_2O_3/GaN device at 245 nm light was determined to be 1.6×10^{11} Jones. The $D*$ of NGr/Ga_2O_3/GaN devices at 235 nm light was determined to be 3.55×10^{12} Jones, as shown in Figure 3d. The improvement of $D*$ is attributed to the reduction of dark current and the increase of responsivity of NGr/Ga_2O_3/GaN devices due to enhancement of the built-in electric field.

JOSarXiv.202303.0003V1

JOSarXiv.202303.0003V1

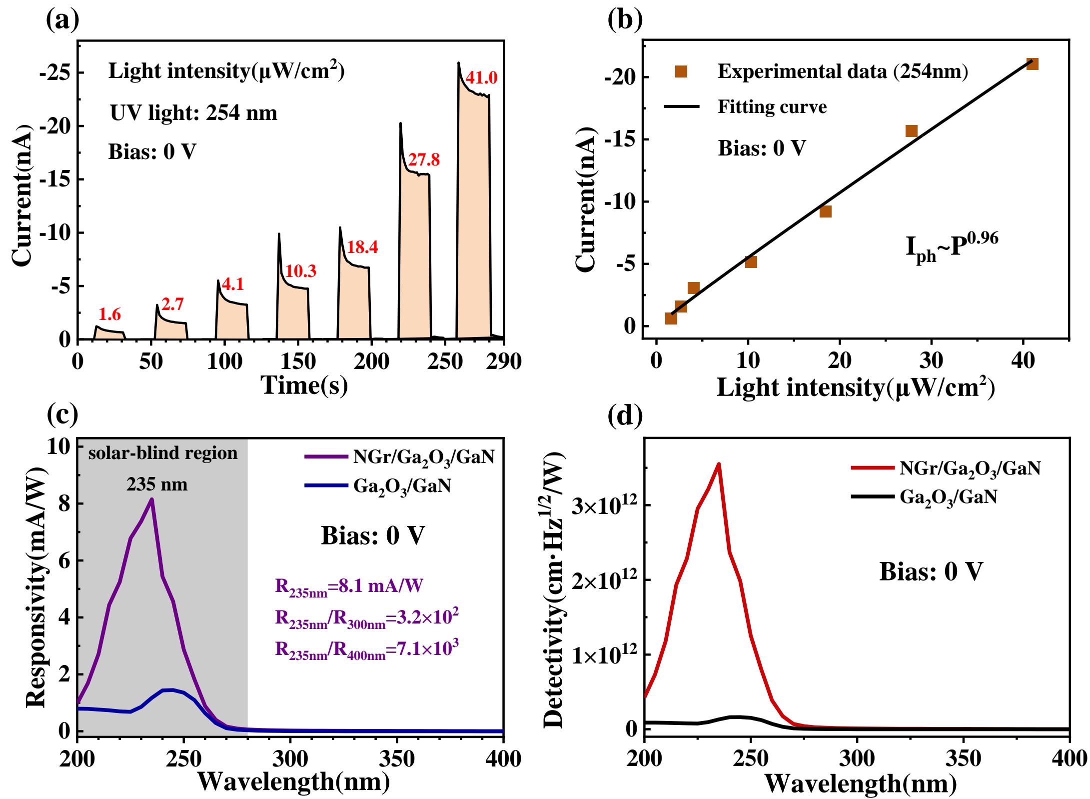

Figure 3. a) The *I-T* curve under 254 nm illumination of different intensities at 0 V bias. b) Fitting curve of photo-current (at 254 nm) vs. light intensity by intensity power law. c) Spectral response of the Ga_2O_3/GaN and NGr/Ga_2O_3/GaN heterojunction photodetectors at 0 V bias. d) Detectivity of the Ga_2O_3/GaN and NGr/Ga_2O_3/GaN heterojunction photodetectors at 0 V bias.

One key parameter for a photodetector is the response speed. This determines its ability to follow a rapidly optical signal. **Figure 4**a shows the transient responses of the detector under 0 V bias voltage and 254 nm light. During the measurement, 254 nm light was repeatedly switched on and off at 20 s time intervals. A stable multicycle time-dependent photocurrent was observed, indicating that the photoelectric performance of the device was repeatable and stable. Figure 4b shows a testing schematic diagram of the device's response speed. A 1 MΩ load resistor was in series with the NGr/Ga_2O_3/GaN heterojunction photodetector. An oscilloscope recorded the bias change of the load resistor. The transient response curve of the oscilloscope was fitted with a double exponential relaxation equation. To obtain the response time of the device, the transient response curves were fitted with a bi-exponential relaxation equation $y = y_0 + A_1 e^{(-t/t_1)} + A_2 e^{(-t/t_2)}$, where y_0 is the steady-state photocurrent, t is time, A_1 and A_2 are constants, and t_1 and t_2 are the relaxation time constants corresponding to two components (fast and slow).[32] Usually, the fast-response component is due to the rapid change of carrier concentration when the light is turned on/off, and the slow-response

component is due to carrier trapping/releasing from defects.[33] As shown in Figure 4c, the decay curves of PD are well fitted, and the rise time and decay time constants under 248 nm laser illumination with 0 V bias are estimated to be 3.2 μs and 0.02/3.49 ms. The response speed of the device is much faster than that of the reported Ga_2O_3 deep-UV device, implying that the device has the potential to be applied in the field of deep-UV detection requiring a fast response.

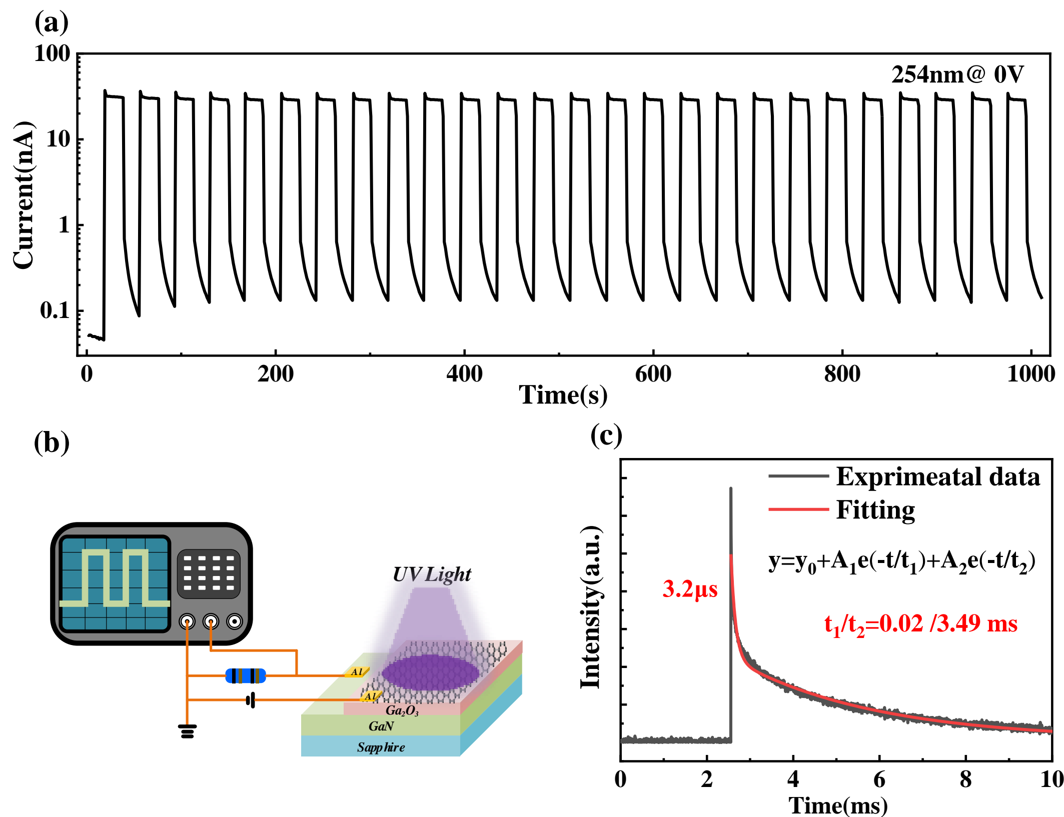

Figure 4. a) The time response curve of the detector under 0 V bias with 254 nm illumination. b) Testing schematic diagram of the device's response speed. c) The time response curve and attenuation fitting curve of a single pulse irradiated by a 248 nm laser with 0 V bias.

In addition to the self-powered response, our detector also had good detection performance under a reverse bias voltage. **Figure 5**a shows the time response curve of the detector under 254 nm illumination with a -5 V bias. The repetitive cycle of multi *I-T* indicates that the detector can also work stably under reverse bias of -5 V. The single cycle response time curve of an oscilloscope is fitted, as shown in Figure 5b. The rise time was 4 μs, and the fall time was 0.9/4.53 ms. Compared with zero bias, the photoresponse time (t_r and t_d) under a reverse bias turned out to be longer. This can be attributed to the electrons and holes captured by the trapping states being released gradually under an applied bias, which would take longer than under zero bias.[34] The responsivity under -5 V bias was calculated, and the results are shown in Figure 5c. The

JOSarXiv.202303.0003V1

peak value of the response spectrum was 8.3 A/W at 250 nm. The UV visible rejection ratio R_{250nm}/R_{400nm} reached 1.6×10^4(as shown in the Figure 5c illustration). D^* reached 8.8×10^{14} Jones under 250 nm illumination with -5 V bias voltage (as shown in Figure 5d). Comparing our NGr/Ga_2O_3/GaN heterojunction device with other previous self-powered solar-blind photodetectors listed in Table 1, it can be found that our device exhibited more desirable responsivity and a high signal-to-noise ratio.

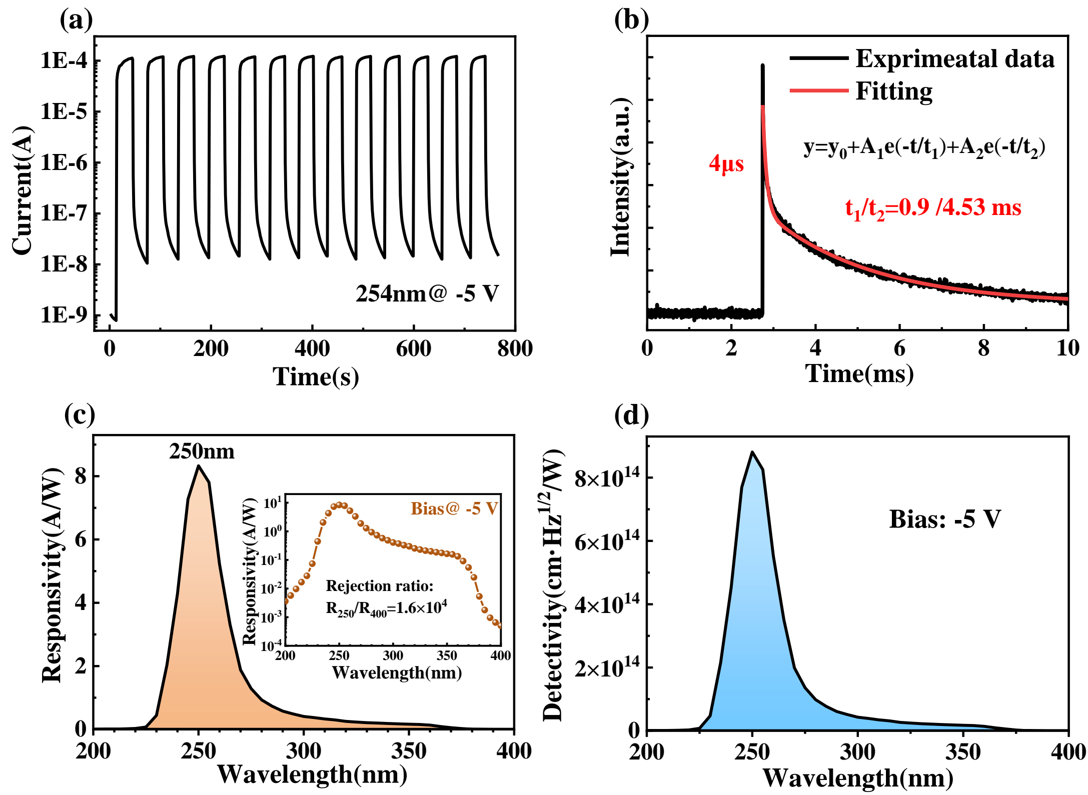

Figure 5. a) The time response curve of the detector under -5 V bias with 254 nm illumination. b) The time response curve and attenuation fitting curve of a single pulse irradiated by a 248 nm laser with -5 V bias. c) The spectral response of a NGr/Ga_2O_3/GaN p-i-n heterojunction photodetector at -5 V bias. The illustration shows the image of responsivity in logarithmic coordinates. d) The D^* of NGr/Ga_2O_3/GaN p-i-n heterojunction photodetector at -5 V bias.

Table 1. Comparison of the performance of photodetectors in this work and other reported devices.

Photodetector	Bias [V]	Responsivity [mA/W]	R_{peak}/R_{400} rejection ratio	Detectivity [Jones]	t_{rise}/t_{decay}	Ref.
$Ga_2O_3/CuMO_2$	0	0.025	2.8×10^4	9×10^{10}	260 ms/140 ms	[35]
β-Ga_2O_3/MoS_2	0	2.05	1.6×10^3	1.21×10^{11}	—	[36]
β-Ga_2O_3/Diamond	0	0.2	1.35×10^2	6.9×10^9	—	[37]
β-Ga_2O_3/PANI	0	21	~10^2	1.5×10^{11}	0.34 ms/8.14 ms	[38]
β-Ga_2O_3/4H-SiC	0	10.35	—	8.8×10^9	11 ms/19 ms	[39]
β-Ga_2O_3/Ag_2O	0	25.65	2.47×10^3	6.1×10^{11}	108 ms/80 ms	[40]
β-Ga_2O_3/GaN	0	28.44	—	6.17×10^{10}	180 ms/80 ms	[17]
Ga:ZnO/Ga_2O_3	0	0.76	>10^2	—	0.179 s/0.272 s	[41]
β-Ga_2O_3/Gr	20	39.3×10^3	—	5.92×10^{13}	~84 s/~219 s	[42]

JOSarXiv.202303.0003V1

n-Si/β-Ga_2O_3	-20	~25	49.4	—	0.2 s/0.02 s	[43]
Gr/Ga_2O_3	-5	185	3×10^4	—	9 ms/8 ms	[44]
NiO/Ga_2O_3	10	27.43×10^3	—	3.14×10^{12}	—	[45]
NGr/Ga_2O_3/GaN	0	8.1	7.1×10^3	3.55×10^{12}	3.2 μs/0.02 ms	This work
NGr/Ga_2O_3/GaN	-5	8.3×10^3	1.6×10^4	8.8×10^{14}	4 μs/0.9 ms	This work

Figure 6a presents the absorption spectra of βGa_2O_3 and GaN thin films. Two distinct absorption edges can be observed in the UV light region. The band-gaps of βGa_2O_3 and GaN were estimated using Tauc plots, whose values extracted from the plot of $(\alpha h\nu)^2$ versus $h\nu$ were ~4.8 eV and ~3.4 eV for βGa_2O_3 film and GaN film, respectively.[46] Figure 6b shows the XPS VB photoelectron spectrum of GaN and βGa_2O_3 thin films. The valence band maximum (VBM) position was determined by linear extrapolation of the leading edge of the valence band spectrum to the base-lines. The energy difference between the Fermi level and the top of the valence band was calculated to be about 2.2 eV of βGa_2O_3. According to the band gap width of βGa_2O_3 in Figure 6a, the Fermi level lay below the center of the band gap, closer to the top of the valence band. The results show that βGa_2O_3 films grown by GaN thermal oxidation were p-type conductive. This is attributed to acceptor doping of N elements in GaN to Ga_2O_3. Thermal oxidation of GaN to p-type βGa_2O_3 has been reported.[47-48] The Fermi level of GaN film was located at 2.1 eV above the VBM, which is closer to the conduction band. It indicates that GaN is n-type conductive. Figure 6c shows the *I-V* curve of NGr in contact with βGa_2O_3 film. The nearly linear *I-V* curve shows that NGr had ohmic contact with βGa_2O_3, and NGr acteds as a hole transport layer.

In order to further understand the photoresponse mechanism of the detector, based on the above-discussed results, the band diagram of NGr/Ga_2O_3/GaN p-i-n heterojunction was drawn, as shown in Figure 6d. The electron affinity potentials of βGa_2O_3 and GaN were 4.0 eV and 4.1 eV, respectively.[22] Under the thermal equilibrium condition, the depletion layer could be formed by the diffusion of majority carriers between βGa_2O_3 and GaN. Due to the high resistance of our thermally oxidized βGa_2O_3 films, the carrier concentrations differed significantly between βGa_2O_3 and GaN. Almost all of the depletion layer was on the βGa_2O_3 side. When ultraviolet light shone on the βGa_2O_3 window layer, the electron-hole pairs generated in βGa_2O_3 were separated rapidly by the built-in electric field existing in the contact interface of the two materials. Based on the continuous conduction band structure of the p-βGa_2O_3/n-GaN heterostructure and the large electron mobility of GaN, electrons were rapidly

JOSarXiv.202303.0003V1

transported to the electrode. Due to the existence of the NGr hole transport layer, the hole carriers in βGa_2O_3 are quickly collected by NGr and transmitted to the external circuit, which reduced the recombination probability of the photogenerated carriers within βGa_2O_3 and thereby greatly increased the photocurrent. Thus, the high responsivity of our solar-blinded photodetector was obtained.

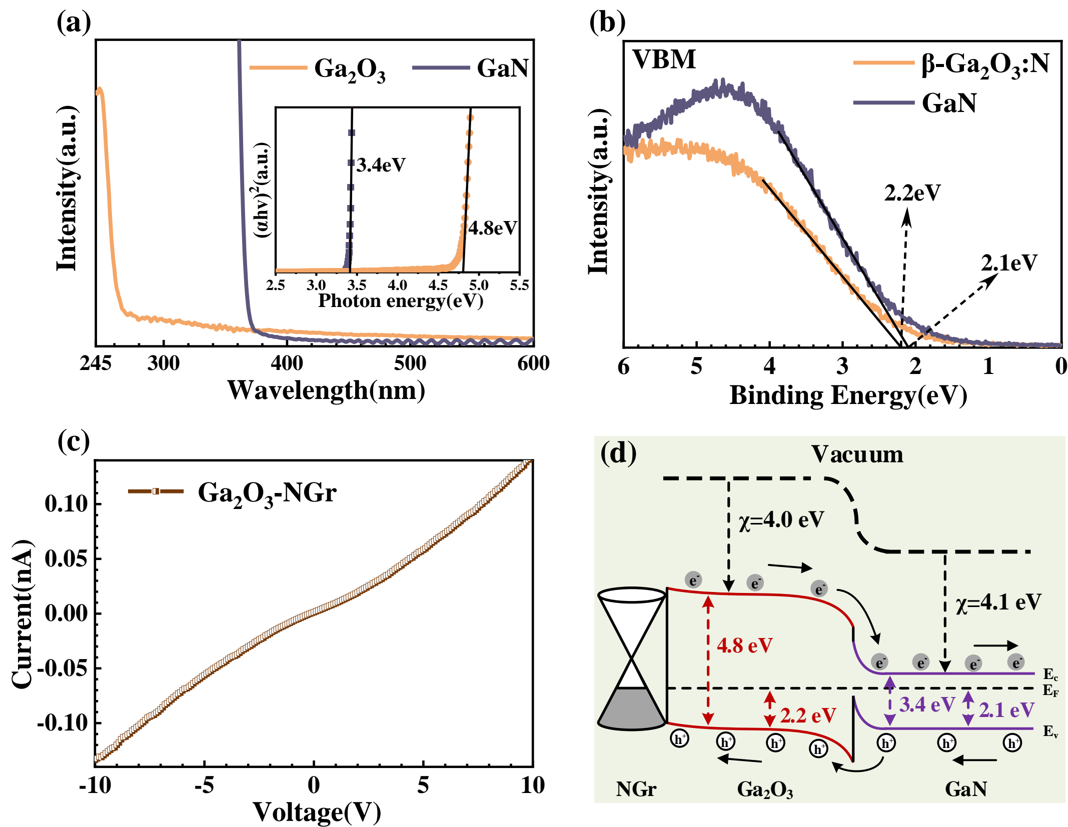

Figure 6. a) The absorption spectra of Ga_2O_3 film and GaN film. Inset: The optical band-gaps of βGa_2O_3 and GaN. b) The XPS VBM of βGa_2O_3 film and GaN film. c) The *I–V* curve of the NGr with βGa_2O_3 films. d) The heterojunction energy band diagram of NGr/Ga_2O_3/GaN.

Conclusion

In conclusion, by transferring p-type N-doped graphene onto a thermally oxidized Ga_2O_3/GaN heterojunction, a NGr/Ga_2O_3/GaN p-i-n heterojunction self-powered solar blind UV photodetector was successfully prepared. Based on the strong hole transmission capability of NGr, the responsivity of the NGr/Ga_2O_3/GaN detector reached 8.1 mA/W at 235 nm. Compared to a Ga_2O_3/GaN heterostructure without NGr, the responsivity was improved 5.7 times. It had a detectivity of more than 10^{12} Jones and a high UV-visible light suppression ratio of 7.1×10^3. The detector also showed good detection performance under a reverse bias voltage. The responsivity was 8.3 A/W, and the detection rate exceeded 10^{14} Jones under -5 V bias voltage. The response speed

JOSarXiv.202303.0003V1

of the device reached the microsecond level. This work provides a feasible method to improve the performance of the UV PDs.

Experimental

Undoped GaN thin films with a thickness of 4 μm were grown epitaxially on Al_2O_3 substrates by MOCVD. The GaN was n-type with a carrier concentration of 2×10^{17} cm^{-3} and mobility of 2.2×10^{2} cm^{2} V^{-1} s^{-1}. After ultrasonic cleaning sequentially with acetone, alcohol, and deionized water, GaN was thermally oxidized in oxygen ambient at 800 °C /900 °C /1000 °C for 8–120 min, respectively. At high temperatures, oxygen atoms take the place of nitrogen atoms in the GaN matrix and turn it into βGa_2O_3. To fabricate UV PDs with p-n heterojunctions, part of the βGa_2O_3 was etched with hot phosphoric acid to expose the underlying GaN. The typical PMMA-assisted wet transfer method was used to transfer N-doped Gr from a Cu substrate to βGa_2O_3 thin film. Al electrodes were deposited on the NGr and GaN thin films by thermal evaporation.

The structure, crystallinity, and orientation of the films were characterized using an X-ray diffractometer (XRD) (Rigaku Ultima IV). Absorption spectroscopy was performed using a Hitachi UH4150 spectrophotometer. The valence band characteristics of the βGa_2O_3 and GaN thin films were investigated by X-ray photoelectron spectroscopy (XPS). A field emission scanning electron microscope (FEI Quanta FEG 250) was used to show the surface morphology and profile of the thin film cross-section. To characterize the photoelectric performance of the PDs, a photoelectric test system comprising a Xe lamp, a monochromator, an optical chopper, and a Keithley 4200 parameter analyzer was used to measure the light response of the devices (*I*-*V* and *I*-*T* characteristics). The response speed tested the capability of the device to follow a rapidly varying optical signal from a KrF excimer laser (λ = 248 nm). During the measurement, a 1 MΩ load resistor was connected with a p-n heterojunction photodetector and an oscilloscope was used to record the bias change of the load resistor.

Acknowledgements

This work was supported by the National Key Technologies Research and Development Program of China under Grant 2019YFA0705202 and the National Natural Science Foundation of China under Grant 62274027 and 31701296.

JOSarXiv.202303.0003V1

Conflict of Interest

The authors declare no conflict of interest.

Data Availability Statement

The data that support the findings of this study are available from the corresponding author upon reasonable request.

Keywords: solar blind deep UV photodetector, βGa_2O_3, GaN, p-i-n heterojunction, reversed substitution growth

References

[1] H. Chen, K. Liu, L. Hu, A. A. Al-Ghamdi, X. Fang, *Mater. Today* **2015**, 18, 493.

[2] S. E. Mancebo, S. Q. Wang, *Rev. Environ. Health* **2014**, 29, 265.

[3] B. Zhao, F. Wang, H. Chen, L. Zheng, L. Su, D. Zhao, X. Fang, *Adv. Funct. Mater.* **2017**, 27, 1700264.

[4] G. Zeng, X. X. Li, Y. C. Li, D. B. Chen, Y. C. Chen, X. F. Zhao, N. Chen, T. Y. Wang, D. W. Zhang, H. L. Lu, *ACS Appl. Mater. Inter.* **2022**, 14, 16846.

[5] Z. Yan, S. Li, J. Yue, Z. Liu, X. Ji, Y. Yang, P. Li, Z. Wu, Y. Guo, W. Tang, *ACS Appl. Mater. Inter.* **2021**, 13, 57619.

[6] Z. Wang, W. Zheng, Q. Hu, S. Lin, Y. Wu, D. Ye, *ACS Appl. Mater. Inter.* **2021**, 13, 44568.

[7] F. Teng, K. Hu, W. Ouyang, X. Fang, *Adv. Mater.* **2018**, 30, e1706262.

[8] R. Liu, D. Jiang, Q. Duan, L. Sun, C. Tian, Q. Liang, S. Gao, J. Qin, *Appl. Phys. Lett.* **2014**, 105.

[9] M. Hou, H. So, A. J. Suria, A. S. Yalamarthy, D. G. Senesky, *IEEE Electr. Device. L.* **2017**, 38, 56.

[10] X. Chang, Y.-F. Wang, X. Zhang, Z. Liu, J. Fu, S. Fan, R. Bu, J. Zhang, W. Wang, H.-X. Wang, J. Wang, *Appl. Phys. Express* **2018**, 112, 032103.

[11] K. T. Kim, H. J. Jin, W. Choi, Y. Jeong, H. G. Shin, Y. Lee, K. Kim, S. Im, *Adv. Funct. Mater.* **2021**, 31.

[12] H. So, D. G. Senesky, *J. Phys. D. Appl. Phys.* **2016**, 49.

[13] Y. Duan, S. Zhang, M. Cong, D. Jiang, Q. Liang, X. Zhao, *J. Mater. Chem. C* **2020**, 8, 12917.

[14] W. Wang, Q. Yuan, D. Han, J. Sun, N. Liu, S. Hu, C. Liu, W. Zhang, J. Ye, *IEEE Electr. Device. L.* **2022**, 1.

[15] Y. Zheng, M. N. Hasan, J. H. Seo, *Adv. Mater. Technol-us.* **2021**, 6, 2100254.

[16] In-Hwan Lee*, Tae Geun Kim, Y. Park, *J. Cryst. Growth* **2002**, 234, 305.

[17] P. Li, H. Shi, K. Chen, D. Guo, W. Cui, Y. Zhi, S. Wang, Z. Wu, Z. Chen, W. Tang, *J. Mater. Chem. C* **2017**, 5, 10562.

JOSarXiv.202303.0003V1

[18] Y. Zhang, Y. Li, Z. Wang, R. Guo, S. Xu, C. Liu, S. Zhao, J. Zhang, Y. Hao, *Sci. China Phys. Mech.* **2020**, 63.

[19] T. Oshima, T. Okuno, N. Arai, Y. Kobayashi, S. Fujita, *Jpn. J. Appl. Phys.* **2009**, 48.

[20] Y. Zhou, C. Ahyi, T. Isaacs-Smith, M. Bozack, C.-C. Tin, J. Williams, M. Park, A.-j. Cheng, J.-H. Park, D.-J. Kim, D. Wang, E. A. Preble, A. Hanser, K. Evans, *Solid State Electron.* **2008**, 52, 756.

[21] D. Guo, Y. Su, H. Shi, P. Li, N. Zhao, J. Ye, S. Wang, A. Liu, Z. Chen, C. Li, W. Tang, *ACS Nano* **2018**, 12, 12827.

[22] Q. Feng, G. Yan, Z. Hu, Z. Feng, X. Tian, D. Jiao, W. Mu, Z. Jia, X. Lian, Z. Lai, C. Zhang, H. Zhou, J. Zhang, Y. Hao, *ECS J. Solid State Sc.* **2020**, 9.

[23] H. Wang, J. Ma, L. Cong, D. Song, L. Fei, P. Li, B. Li, Y. Liu, *Mater. Today Phys.* **2022**, 24, 100673.

[24] S. Nakagomi, Y. Kokubun, *J. Cryst. Growth* **2012**, 349, 12.

[25] T. Yamada, J. Ito, R. Asahara, K. Watanabe, M. Nozaki, S. Nakazawa, Y. Anda, M. Ishida, T. Ueda, A. Yoshigoe, T. Hosoi, T. Shimura, H. Watanabe, *J. Appl. Phys.* **2017**, 121.

[26] M. Ai, D. Guo, Y. Qu, W. Cui, Z. Wu, P. Li, L. Li, W. Tang, *J. Alloy. Compd.* **2017**, 692, 634.

[27] Z. Ni, Y. Wang, T. Yu, Z. Shen, *Nano Res.* **2010**, 1, 273.

[28] L. G. Cancado, A. Jorio, E. H. Ferreira, F. Stavale, C. A. Achete, R. B. Capaz, M. V. Moutinho, A. Lombardo, T. S. Kulmala, A. C. Ferrari, *Nano Lett.* **2011**, 11, 3190.

[29] H. Wang, J. Ma, L. Cong, H. Zhou, P. Li, L. Fei, B. Li, H. Xu, Y. Liu, *Mater. Today Phys.* **2021**, 20.

[30] S. Fu, Y. Wang, Y. Han, B. Li, Y. Zhang, J. Ma, Z. Fu, H. Xu, Y. Liu, *IEEE Electr. Device. L.* **2022**, 43, 1511.

[31] L. Cong, H. Zhou, M. Chen, H. Wang, H. Chen, J. Ma, S. Yan, B. Li, H. Xu, Y. Liu, *J. Mater. Chem. C* **2021**, 9, 2806.

[32] D. Zhang, W. Lin, S. Liu, Y. Zhu, R. Lin, W. Zheng, F. Huang, *ACS Appl. Mater. Inter.* **2019**, 11, 48071.

[33] D. Y. Guo, Z. P. Wu, Y. H. An, X. C. Guo, X. L. Chu, C. L. Sun, L. H. Li, P. G. Li, W. H. Tang, *Appl. Phys. Lett.* **2014**, 105, 023507.

[34] D. Guo, H. Liu, P. Li, Z. Wu, S. Wang, C. Cui, C. Li, W. Tang, *ACS Appl. Mater. Inter.* **2017**, 9, 1619.

[35] C. Wu, L. Qiu, S. Li, D. Guo, P. Li, S. Wang, P. Du, Z. Chen, A. Liu, X. Wang, H. Wu, F. Wu, W. Tang, *Mater. Today Phys.* **2021**, 17, 100335.

[36] R. Zhuo, D. Wu, Y. Wang, E. Wu, C. Jia, Z. Shi, T. Xu, Y. Tian, X. Li, *J. Mater. Chem. C* **2018**, 6, 10982.

[37] Y.-C. Chen, Y.-J. Lu, C.-N. Lin, Y.-Z. Tian, C.-J. Gao, L. Dong, C.-X. Shan, *J. Mater. Chem. C* **2018**, 6, 5727.

JOSarXiv.202303.0003V1

[38] Y. Wang, L. Li, H. Wang, L. Su, H. Chen, W. Bian, J. Ma, B. Li, Z. Liu, A. Shen, *Nanoscale* **2020**, 12, 1406.

[39] J. Yu, L. Dong, B. Peng, L. Yuan, Y. Huang, L. Zhang, Y. Zhang, R. Jia, *J. Alloy. Compd.* **2020**, 821.

[40] S. Park, T. Park, J. H. Park, J. Y. Min, Y. Jung, S. Kyoung, T. Y. Kang, K. H. Kim, Y. S. Rim, J. Hong, *ACS Appl. Mater. Inter.* **2022**.

[41] Z. Wu, L. Jiao, X. Wang, D. Guo, W. Li, L. Li, F. Huang, W. Tang, *J. Mater. Chem. C* **2017**, 5, 8688.

[42] W. Y. Kong, G. A. Wu, K. Y. Wang, T. F. Zhang, Y. F. Zou, D. D. Wang, L. B. Luo, *Adv. Mater.* **2016**, 28, 10725.

[43] D. Hu, Y. Wang, Y. Wang, W. Huan, X. Dong, J. Yin, *Mater. Lett.* **2022**, 312, 131653.

[44] T. He, Y. Zhao, X. Zhang, W. Lin, K. Fu, C. Sun, F. Shi, X. Ding, G. Yu, K. Zhang, S. Lu, X. Zhang, B. Zhang, *Nanophotonics* **2018**, 7, 1557.

[45] M. Jia, F. Wang, L. Tang, J. Xiang, K. S. Teng, S. P. Lau, *Nanoscale Res. Lett.* **2020**, 15, 47.

[46] Y. Zhang, Y. Wang, R. Fu, J. Ma, H. Xu, B. Li, Y. Liu, *J. Phys. D Appl. Phys.* **2022**, 55.

[47] Z. Y. Wu, Z. X. Jiang, C. C. Ma, W. Ruan, Y. Chen, H. Zhang, G. Q. Zhang, Z. L. Fang, J. Y. Kang, T. Y. Zhang, *Mater. Today Phys.* **2021**, 17, 100356.

[48] Z. X. Jiang, Z. Y. Wu, C. C. Ma, J. N. Deng, H. Zhang, Y. Xu, J. D. Ye, Z. L. Fang, G. Q. Zhang, J. Y. Kang, T. Y. Zhang, *Mater. Today Phys.* **2020**, 14.

JOSarXiv.202303.0003V1